Research Square

Preprints are preliminary reports that have not undergone peer review.
They should not be considered conclusive, used to inform clinical practice,
or referenced by the media as validated information.

Study on the Corrosion Behavior of a High-Strength and High-Toughness Al-Mg-Si-Cu-Mn-Cr Alloy for Agricultural Applications

Xiaoguo Wang

wxg315550@sxau.edu.cn

Shanxi Agricultural University

Hongxian Wang

Shanxi Agricultural University

Weigang Xue

Shanxi Agricultural University

Jialin Wang

Shanxi Agricultural University

Dongwen Guo

Shanxi Agricultural University

Ruirui Wu

Taiyuan University of Science and Technology

Weiqi Yan

Auckland University of Technology

Article

Keywords: Al-Mg-Si-Cu-Mn-Cr alloy, thermal deformation, electrochemical tests, intergranular corrosion, corrosion mechanism

Posted Date: November 20th, 2026

DOI: https://doi.org/10.21203/rs.3.rs-11543379/v1

License: This work is licensed under a Creative Commons Attribution 4.0 International License.
Read Full License

Additional Declarations: No competing interests reported.

Study on the Corrosion Behavior of a High-Strength and High-Toughness Al-Mg-Si-Cu-Mn-Cr Alloy for Agricultural Applications

Xiaoguo Wang[1,2*], Hongxian Wang [1,2], Weigang Xue[1,2], Jialin Wang[1,2], Dongwen Guo[1,2],Ruirui Wu[3], Weiqi Yan[4]

(1. College of Agricultural Engineering, Shanxi Agricultural University, Taigu 030801, China; 2. Shanxi Key Laboratory of Key Technologies and Equipment for Agricultural Machinery, Taigu 030801, China;3. Analysis and Testing Center, Taiyuan University of Science and Technology, Taiyuan 030024, China; 4. School of Engineering, Computer and Mathematical Sciences, Auckland University of Technology, Auckland 1010, New Zealand)

Corresponding author: Xiaoguo Wang E-mail address: wxg315550@sxau.edu.cn

Abstract: To address the insufficient corrosion resistance of high-strength and high-toughness 6xxx-series Al alloys for agricultural applications under complex and harsh service environments, a micro-alloyed semi-continuously cast alloy Y (Al-0.9Mg-1.1Si-0.6Cu-0.7Mn-0.2Cr) was investigated in this work. The alloy was first subjected to two-stage homogenization heat treatment and then to two thermal deformation routes, i.e., hot compression at 350 - 500 °C and rolling followed by T6 treatment. OM, SEM, EDS, XRD, potentiodynamic polarization, electrochemical impedance spectroscopy (EIS), and intergranular corrosion tests were employed to study the microstructural evolution and corrosion behavior of the alloy and to reveal the corrosion mechanisms under different thermal deformation conditions. The results show that the as-cast alloy consists of α-Al、Mg_2Si、Q($Al_4Cu_2Mg_8Si_7$)及 Al(Fe,Mn,Cr)Si phases. After homogenization heat treatment, fine dispersed precipitates form, which not only inhibit grain coarsening but also act as micro-galvanic corrosion sites. The hot compression temperature exerts a significant regulatory effect on the corrosion resistance of the alloy. Combined analysis of the potentiodynamic polarization curves and EIS results indicates that when the hot compression temperature is 400 °C, the corrosion current density (I_{corr}) of the alloy reaches its minimum value of $7.17216\times10^{-6}A\cdot cm^{-2}$, and the alloy exhibits the optimal comprehensive corrosion resistance. Meanwhile, the intergranular corrosion of the rolled + T6 alloy is dominated by localized pitting and exfoliation, which is related to the local galvanic coupling of precipitates and defects in the passive film. This study provides a basis for the corrosion resistance control during hot processing and the long-life design of aluminum alloys for agricultural applications.

Keywords: Al-Mg-Si-Cu-Mn-Cr alloy; thermal deformation; electrochemical tests; intergranular corrosion; corrosion mechanism

1.Introduction

Against the backdrop of “carbon peaking and carbon neutrality,” lightweight design and long-life design have become core requirements for the green development of agriculture[1]. Aluminum alloys, owing to their low density, high specific strength, and good recyclability, have become an important material choice for the lightweighting of agricultural machinery. In the field of agricultural machinery, Lü Xinyu[2] used 6B63 aluminum alloy to develop sprinkler irrigation pipes; after combined die extrusion–water spray quenching–aging, the tensile strength increased from 115 - 140 MPa to 232 - 245 MPa, and the intergranular corrosion resistance reached grade 1. Zheng Siyi[3] found that the aluminum alloy pulley of a KCKY-6 combine harvester exhibited a wear loss of 0.8 - 1.2 mm in one season, and pointed out that micro-arc oxidation can in situ grow an oxidized ceramic layer, significantly improving wear and corrosion resistance. In addition, as early as the 1980s, foreign studies employed high-frequency welded aluminum pipes for agricultural irrigation, increasing grain yield per hectare by more than twofold[4]. E.J. Qilaika et al.[5] exposed 5086, 5083, and 5456 aluminum alloys to a marine environment for two years; no

exfoliation corrosion occurred, and the full-immersion corrosion rate decreased from 0.80 to 0.39 mils per year, providing analogous data for long-term corrosion resistance in humid salt-spray environments of farmland. Lancaster et al.[6] added 10 wt.% walnut shell particles to 6063 aluminum alloy, increasing the hardness from 104.94 kgf/mm^2 to 109.24 kgf/mm^2 and substantially reducing the corrosion rate from 0.7321 to 0.1336 mm/year, thereby achieving a synergistic improvement in mechanical properties and corrosion resistance and providing a new idea for the green modification of agricultural aluminum alloys.

However, farmland service environments are complex. Factors such as water and fertilizer (acids, alkalis, and salts), pesticide residues, soil abrasive particles, alternating wet–dry conditions, and galvanic effects can readily damage the passive film on 6xxx-series aluminum alloys, triggering pitting corrosion, intergranular corrosion, galvanic corrosion, and even stress corrosion cracking, and ultimately leading to premature failure of structural components. If the corrosion resistance is insufficient, the weight-saving benefits of lightweighting will be offset by frequent maintenance, replacement, and premature scrapping, making the goals of long service life and remanufacturability difficult to achieve.

Although high-strength and high-toughness 6xxx-series aluminum alloys can achieve relatively high strength and toughness through microalloying and heat treatment, the precipitation of strengthening phases, grain-boundary microstructure, and residual stress often simultaneously affect corrosion susceptibility, and there is a complex trade-off between strength–toughness and corrosion resistance. For example, Zhang et al.[7] used in situ AFM to observe in real time the initiation and propagation of pitting corrosion of 6061 aluminum alloy in 3.5% NaCl solution, and found that pitting preferentially initiates around Mg_2Si precipitates and that the adsorption of Cl− is a key factor leading to passive film breakdown. Li et al.[8] combined quantum chemical calculations with electrochemical tests and revealed that the essence of intergranular corrosion in 6xxx-series aluminum alloys is the potential difference between grain-boundary precipitates (Mg_2Si, Al_2CuMg) and the matrix, which forms micro-galvanic cells and leads to preferential dissolution of grain boundaries. Regarding the pitting mechanism, most SCI studies suggest that Cl^- penetrates defect sites in the passive film, disrupting film integrity and forming pitting nuclei, which then gradually develop into pits, while low-oxygen environments such as the deep sea significantly accelerate the pitting process[9][10]. In addition, studies on stress corrosion cracking have shown that the synergistic effect of tensile stress and corrosive media leads to crack initiation and propagation, and that the size and distribution of Mg_2Si precipitates significantly affect stress corrosion susceptibility[11]. At present, research on agricultural 6xxx-series aluminum alloys has mostly focused on lightweight substitution and mechanical property improvement, whereas studies on the corrosion behavior and mechanisms of high-strength and high-toughness aluminum alloys in complex farmland service environments remain relatively limited, and the microstructure–property correlation is still unclear. In this paper, a high-strength and high-toughness 6xxx-series aluminum alloy for agricultural applications was taken as the research object. Electrochemical tests and intergranular corrosion experiments were conducted to analyze the corrosion types, influencing factors, and microstructure–corrosion resistance correlation of the alloy in simulated typical farmland environments from the perspective of the correlations among thermal processing, microstructure, electrochemical corrosion, and intergranular corrosion behavior, aiming to provide a theoretical basis for the long-life design and full-life-cycle resource conservation of green agricultural machinery equipment.

2. Experimental Materials and Methods

2.1 Sample Preparation

The samples used in this study were ingots of a novel high-strength and high-toughness 6xxx-series aluminum alloy prepared by microalloying combined with semi-continuous casting, and the alloy was designated as alloy Y. Its nominal composition is listed in Table 1.

Table 1. Chemical composition of the novel high-strength and high-toughness aluminum alloy

Alloy	Mg	Si	Cu	Mn	Cr	Al
Y	0.9	1.1	0.6	0.7	0.2	Bal

2.1 Sample Preparation

To regulate the as-cast microstructure, the as-cast alloy Y was subjected to a two-stage homogenization heat treatment schedule, as listed in Table 2. Subsequently, the homogenized alloy was cut into two parts using a DK7735 CNC wire electrical discharge machining machine. One part was cut into hot compression specimens with dimensions of ϕ10 mm × 15 mm and then subjected to hot compression tests on a Gleeble-3800 system. The selected hot deformation temperatures (T) were 350, 400, 450, and 500 °C, the strain rate ($\dot{\varepsilon}$) was 0.1 s^{-1}, and the true strain was set to 0.9. After testing, the specimens were water-quenched to preserve the microstructure formed during high-temperature deformation. In addition, another part of the alloy after two-stage homogenization heat treatment was milled to remove surface casting defects and wire-cut into billets of 100 mm × 45 mm × 20 mm. The billets were held at 500 °C for 1 h and then hot-rolled: the hot rolling temperature was set at 450 °C, with a 10-min holding at 450 °C between passes. A total of six passes of hot rolling and cold rolling were performed, and the alloy was finally rolled to a thickness of 3 mm; the rolling process is listed in Table 3. The rolled alloy sheets were then subjected to T6 heat treatment, with the process listed in Table 2.

Table 2. Heat treatment experimental schemes

Heat treatment schedule	Heat treatment process
Two-stage homogenization heat treatment	300℃×8 h + 550℃×10 h
T6 heat treatment	520℃×0.5 h + 180℃×5 h

Table.3 Rolling Process

Rolling method	Pass	Entry thickness/mm	Exit thickness/mm	Pass Reduction/mm	Total Reduction/%
Hot rolling	1	20	14	6	30
	2	14	9	5	55
	3	9	6	3	70
	4	6	5	1	75
Cold rolling	5	5	4	1	80
	6	4	3	1	85

Note: Hot rolling deformation rate: 70%; Cold rolling deformation rate: 50%

2.2 Electrochemical Tests

The central portion of the hot-compressed specimens was cut out, sequentially ground with abrasive papers, rinsed with deionized water, and dried. A copper wire was then connected, and the specimens were sealed with epoxy resin for electrochemical testing. The test results were fitted using an R_s-(CPE_1-R_1)-(CPE_2-R_2) equivalent circuit, as shown in Fig. 1. In this study,

electrochemical tests were performed using a Corrtest CS2350M dual potentiostat. The test objects were samples prepared after hot compression deformation at different temperatures and a strain rate of 0.1 s^{-1}. A saturated calomel electrode (SCE) was used as the reference electrode, a platinum sheet as the counter electrode, and the samples corresponding to the strain rate of 0.1 s^{-1} at different temperatures as the working electrode, with an exposed area of 1 cm^2. The potential range was −1.2 to −0.2 V, the scan rate was 1 mV/s, and the test solution was 3.5 wt.% NaCl solution.

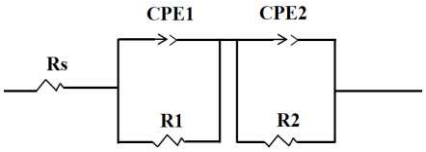


Fig. 1. Equivalent circuit diagram

2.3 Intergranular Corrosion Tests

The alloy sheets after T6 heat treatment were cut into standard specimens of 20 mm × 20 mm × 3 mm by wire electrical discharge machining. The specimens were sequentially ground with abrasive papers from 240# to 1500#, with deionized water continuously used for cooling during grinding to avoid overheating defects on the specimen surfaces. After grinding, the specimen surfaces were thoroughly rinsed with deionized water to remove surface grinding debris, then immersed in anhydrous ethanol for 5 min for dehydration, and finally dried with cold air. Intergranular corrosion susceptibility testing was conducted in accordance with GB/T 7998—2023 Evaluation method for intergranular corrosion susceptibility of aluminum alloys. The temperature of the corrosion solution was maintained at 35 ± 1 °C, the distance between the specimen and the liquid surface was no less than 20 mm, and the immersion time was 24 h. Three parallel specimens were set up for the experiment. After immersion, the corroded specimens were observed by optical microscopy to examine their corrosion morphology.

3. Results and Analysis

3.1 Microstructural morphology analysis of the as-cast alloy

Using the composition listed in Table 1 as the design basis, alloy Y ingots were prepared via a semi-continuous casting route. It should be noted that Fe is not an intentionally added constituent in the composition design but rather a trace impurity introduced by the inherent purity of the industrial pure aluminum raw material and by contact with tooling such as the melting crucible and casting mold. Consequently, residual Fe at extremely low levels is still difficult to completely avoid in the alloy Y ingot. To clarify the microstructural characteristics of the as-cast alloy Y, a stepwise OM–SEM–XRD characterization route was established in this work to analyze the morphology, micro-area composition, and phase constitution of the as-cast specimens.

Low-magnification bright-field observation was performed by OM, and Fig. 2 shows the as-cast microstructure of alloy Y. Eutectic phases formed during non-equilibrium solidification are distributed both at grain boundaries and within grains. The overall microstructure can be classified into four types: the α-Al matrix, a grayish-white spherical phase, a gray eutectic phase between dendrite arms, and a black elongated phase. In addition, eutectic colonies are visible near the grain boundaries, and their formation is closely related to non-equilibrium crystallization under casting conditions.

Because OM has limited capability in identifying the types of second phases, SEM combined with EDS was further employed for high-magnification morphological observation and qualitative

and semi-quantitative micro-area elemental analysis. Fig. 3 presents the EDS point analysis results for three typical second phases in the as-cast alloy. The grayish-white spherical phase A has a relatively high Cu content and is inferred to be a Cu-containing Q phase. The black strip-like phase B contains Mg and Si and is inferred to be the primary Mg_2Si phase. The grayish-white elongated phase C contains Mn, Cr, and Si, consistent with the compositional characteristics of the α-Al(Fe,Mn,Cr)Si phase; the Cu and Mg detected in phase C may be related to non-equilibrium solidification.

To eliminate the contingency of micro-area analysis and to verify the phase composition as a whole, XRD analysis was performed on the as-cast alloy, and the results are shown in Fig. 5. Phase identification of the XRD peaks indicates that the main phases in the as-cast alloy Y include primary Mg_2Si, the Q ($Al_4Cu_2Mg_8Si_7$) phase, and Fe-, Mn-, and Cr-containing $Al_5(Fe,Mn,Cr)Si$ and $Al_8(Fe,Mn,Cr)_2Si$ phases, which are consistent with the SEM morphology observations and EDS identification results. Because the Cu addition level is relatively low, the precipitated fraction of the Q phase is limited, and thus its diffraction peak intensity is weak[12]. In as-cast 6xxx-series aluminum alloys, the solid solubility of Fe in the α-Al matrix is extremely low; therefore, during solidification, Fe is prone to solute enrichment ahead of the solid/liquid interface and precipitates in the form of constituent phases in the interdendritic regions or at grain boundaries. It should be noted that such Fe-rich constituent phases are not ideal stoichiometric binary Al-Fe-Si phases; their crystal lattices can accommodate a certain amount of transition elements such as Mn and Cr, accompanied by partial atomic site substitution. Studies by Liu Hong et al.[13] and Zhang Xinming et al.[14] on aluminum alloys containing Fe, Mn, and Cr further indicated that during the formation of constituent phases in 6xxx-series aluminum alloys, Mn, Fe, and Cr exhibit a mutual substitution relationship and can replace some Fe sites in the Al-Fe-Si phases, thereby forming constituent phases such as $Al_5(Fe,Mn,Cr)Si$ and $Al_8(Fe,Mn,Cr)_2Si$.

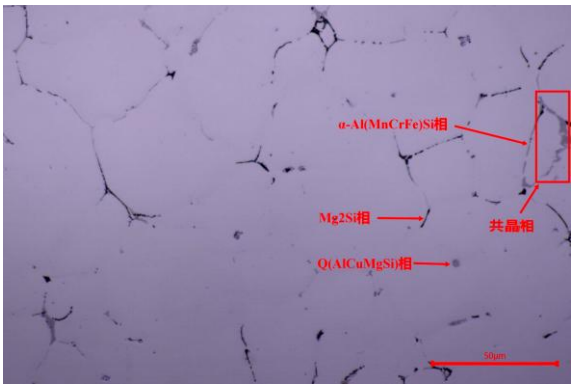


Fig. 2. Optical micrograph of the as-cast alloy.

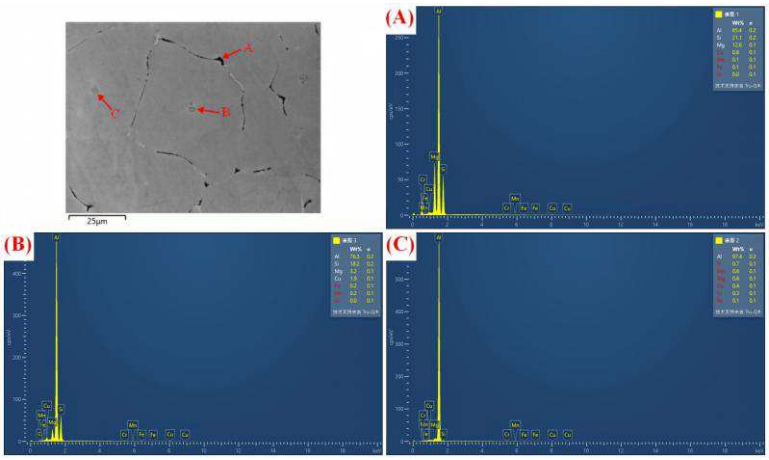


Fig. 3. SEM micrographs of the as-cast alloy.

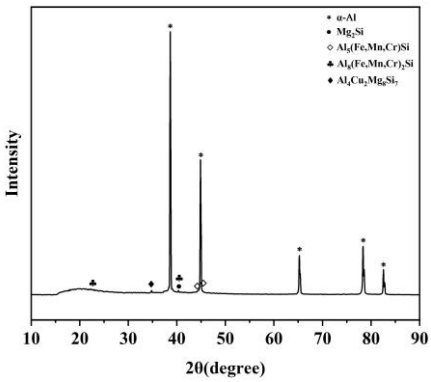


Fig. 4. XRD patterns of the as-cast alloy.

3.1 Electrochemical Tests

After two-stage homogenization treatment, a high density of dispersed precipitates forms within the matrix of the 6xxx-series aluminum alloy, and this microstructural state constitutes the key microstructural basis for its electrochemical corrosion response. The two-stage homogenization promotes sufficient diffusion of solute elements such as Mg, Si, Cu, Mn, and Cr and leads to the formation of fine dispersoids such as Al(Fe,Mn,Cr)Si, Mg_2Si, and AlCuMgSi, as shown in Fig. 5. On the one hand, such particles restrict coarsening of the matrix grains and reduce the degree of elemental segregation at grain boundaries, thereby exerting a certain inhibiting effect on intergranular corrosion. On the other hand, their potential difference from the aluminum matrix enables them to act as cathodic phases for microgalvanic corrosion, constituting an intrinsic cause of corrosion initiation. Therefore, clarifying the differences in corrosion behavior of alloy Y under different hot deformation conditions and the underlying microstructural influence mechanisms is of key value for optimizing corrosion resistance control in practical production.

On this basis, to simulate the actual hot working process and investigate the effects of different deformation temperatures on the microstructure and corrosion resistance, hot compression experiments were performed on the homogenized alloy at 350, 400, 450, and 500 °C to prepare specimens in different hot-deformed states. During hot deformation, the degree of dynamic recrystallization and the precipitation behavior of second phases (such as Cu-containing phases and Mg_2Si) change significantly with temperature, thereby profoundly affecting the integrity of the surface film and the microgalvanic corrosion kinetics of the matrix.

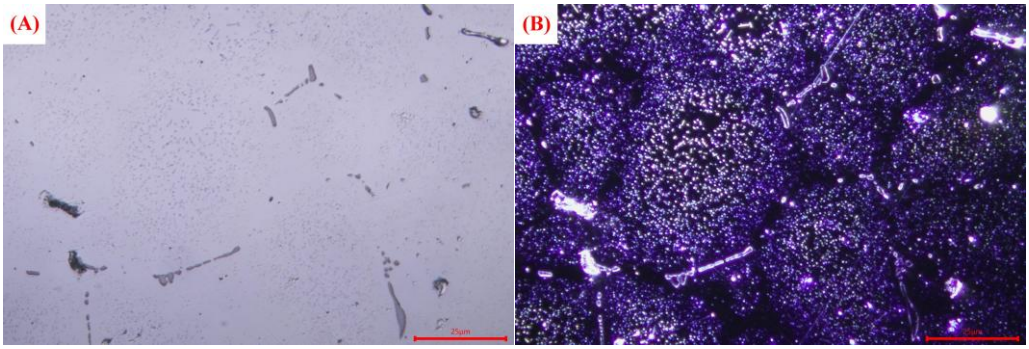


Fig. 5. Optical microscope images of the homogenized microstructure: (A) bright-field image; (B) dark-field image.

3.1.1 Potentiodynamic Polarization Tests

After two-stage homogenization treatment, a high density of dispersed precipitates forms within the matrix of the 6xxx-series aluminum alloy, and this microstructural state constitutes the key microstructural basis for its electrochemical corrosion response. Two-stage homogenization promotes sufficient diffusion of solute elements such as Mg, Si, Cu, Mn, and Cr and leads to the formation of fine dispersoids such as Al(Fe,Mn,Cr)Si, Mg_2Si, and AlCuMgSi. On the one hand, such particles restrict coarsening of the matrix grains and reduce the degree of elemental segregation at grain boundaries, thereby exerting a certain inhibiting effect on intergranular corrosion. On the other hand, their potential difference from the aluminum matrix enables them to act as cathodic phases for microgalvanic corrosion, constituting an intrinsic cause of corrosion initiation. Therefore, clarifying the differences in corrosion behavior of alloy Y under different hot deformation conditions and the underlying microstructural influence mechanisms is of key value for optimizing corrosion resistance control in practical production.

Potentiodynamic polarization tests were used to characterize the corrosion response of the test samples under different hot deformation temperatures. Fig. 6 shows the potentiodynamic polarization curves obtained at 350 - 500 °C and a strain rate of 0.1 s^{-1}. All four polarization curves exhibit typical polarization characteristics within the test range, indicating that the corrosion behavior under the various processes is relatively similar. The potential corresponding to the minimum corrosion current on the curves is the corrosion potential (E_{corr}). Linear fitting of the cathodic and anodic branches was performed over a 60 - 120 mV interval near the corrosion potential, and the corrosion current density (I_{corr}) was obtained by Tafel extrapolation. E_{corr} reflects the thermodynamic stability and corrosion tendency: the more negative the value, the more pronounced the corrosion tendency. I_{corr} provides parameter support for characterizing the corrosion kinetics and is positively correlated with the corrosion rate: the lower the value, the better the corrosion resistance. Therefore, excellent corrosion resistance requires the material to possess both a relatively high E_{corr} and a relatively low I_{corr}[15].

Table 4 summarizes the two core electrochemical parameters, E_{corr} and I_{corr}, obtained by fitting the polarization curves of the alloy samples at different temperatures. Among them, the alloy hot-compressed at 400 °C exhibits the lowest I_{corr}, 7.17216×10^{-6} A·cm^{-2}, while the alloy hot-compressed at 450 °C exhibits the highest I_{corr}, 1.06962×10^{-5} A·cm^{-2}. As can be seen from the table, the corrosion resistance of the specimens at different temperatures decreases in the order: 400 °C > 500 °C > 350 °C > 450 °C. The above differences in corrosion resistance are not determined solely by a single electrochemical parameter but are a macroscopic manifestation of

the differences in the alloy microstructure, especially the microgalvanic interaction between grain-boundary precipitates and the matrix.

Intergranular corrosion in 6xxx-series aluminum alloys originates from the formation of a corrosion galvanic cell between grain-boundary precipitates and the α-Al matrix, which induces selective dissolution of the grain-boundary regions. Li et al.[16], Wang et al.[17], and Kairy[18] pointed out that E_{corr} is not determined by a single factor but is jointly regulated by the solute concentration of the matrix, the spatial distribution of second-phase particles, and grain-boundary characteristics. The coexistence of Mg, Si, Cu, Mn, and Cr in alloy Y enables the precipitation of second-phase particles such as Mg_2Si, Q (AlCuMgSi), and Al(Fe,Mn,Cr)Si; the electrochemical potential differences between these particles and the α-Al matrix can form microgalvanic cells, which become the driving force for localized corrosion.

At a hot compression temperature of 350 °C, the relatively low temperature makes dynamic recovery and recrystallization difficult to proceed sufficiently, so the dislocation density, subgrain boundary density, and residual stress all remain at relatively high levels; meanwhile, solute diffusion kinetics are limited and microstructural homogenization is insufficient, making elemental segregation and non-uniform distribution of precipitates prone to occur near grain boundaries. The passive film in such high-energy defect regions is less stable, and Cl^- is readily adsorbed and penetrates the passive film, becoming the preferential nucleation sites for pitting corrosion and thus accelerating corrosion[19].

Although the sample hot-compressed at 400 °C has the most negative E_{corr} and thus a relatively large thermodynamic driving force for corrosion, its I_{corr} is the lowest, indicating that the actual corrosion rate is more governed by the microstructural state. At this temperature, the microstructural uniformity may be relatively good, the precipitates are fine and dispersed, grain-boundary segregation is weak, the microgalvanic effect is alleviated, and the passive film is relatively complete and stable, providing the best protection for the matrix.

The sample hot-compressed at 450 °C exhibits the poorest corrosion resistance, mainly because its corrosion kinetics rate is the highest rather than because its thermodynamic corrosion tendency is the greatest. This temperature may lie in the sensitive range for precipitation and coarsening of second phases, in which second phases such as Mg_2Si, Q (AlCuMgSi), and Al(Fe,Mn,Cr)Si readily coarsen and distribute continuously along grain boundaries; the potential differences between these phases and the α-Al matrix form microgalvanic cells, in which Cu-containing phases can act as cathodes and promote anodic dissolution of the matrix, aggravating intergranular corrosion and pitting corrosion[20].

At a hot compression temperature of 500 °C, dynamic recrystallization is more complete and microstructural uniformity is improved; some coarse precipitates may re-dissolve, and a supersaturated solid solution is obtained after water quenching, so the number of coarse cathodic phases decreases and the microgalvanic corrosion effect is weakened. Therefore, its corrosion resistance is significantly higher than that of the samples hot-compressed at 350 °C and 450 °C; however, compared with the sample hot-compressed at 400 °C, the I_{corr} of the 500 °C sample is still slightly higher, indicating that a small amount of residual precipitates or locally non-uniform regions may remain in the microstructure, and thus its corrosion resistance is slightly lower than that of the 400 °C sample.

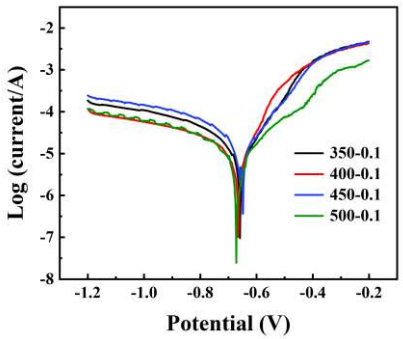


Fig. 6. Potentiodynamic polarization curves.

Table 4. Polarization data of the alloy under different hot compression conditions.

Sample	Corrosion potential (V)	Corrosion current density (10^{-6} A·cm^{-2})
350℃	-0.64294	8.57308
400℃	-0.64338	7.17216
450℃	-0.63754	10.6962
500℃	-0.64332	7.81222

3.1.2 Electrochemical Impedance Spectroscopy Tests

To further analyze the interfacial electrochemical response and corrosion mechanisms of alloy Y under different hot deformation temperatures, electrochemical impedance spectroscopy (EIS) tests were carried out on the four specimens in 3.5% NaCl solution, and the results are shown in Fig. 7.

As can be seen from the Nyquist plot in Fig. 7(A), all four specimens exhibit distinct double capacitive arc characteristics; this phenomenon is corroborated by the Bode plot in Fig. 7(B), in which the phase angle curves show two obvious peaks, corresponding to two time constants. The high-frequency capacitive arc (high-frequency phase angle peak) corresponds to the interfacial electrochemical response between the alloy surface film and the electrolyte, while the low-frequency capacitive arc (mid-to-low-frequency phase angle peak) reflects the localized corrosion and charge transfer processes at the interface between the alloy matrix and the surface. The Bode plot shows that the maximum phase angle of each specimen is approximately 60°, exhibiting typical non-ideal capacitive characteristics, which provides a basis for using a constant phase element (CPE) instead of a pure capacitor. From the low-frequency impedance modulus (|Z| at 10^{-2} Hz) in the Bode plot, the specimens rank from high to low as follows: 500 °C > 400 °C > 350 °C > 450 °C, which is highly consistent with the capacitive arc radius in the Nyquist plot. It is noteworthy that the 350 °C specimen does not converge smoothly at the low-frequency end but instead exhibits a weak inductive loop feature, indicating that the local passive film in this state has a tendency toward breakdown and pitting initiation.

The R_s-(CPE_1-R_1)-(CPE_2-R_2) equivalent circuit shown in Fig. 1 was used to fit the EIS data[21]. Due to the roughness of the actual electrode surface and the non-uniform current distribution, the constant phase element (CPE) was used instead of a pure capacitor to account for the non-ideal capacitive behavior of the electric double layer and corrosion products. In this model, R_s is the solution resistance; R_1 and CPE_1 characterize the surface film resistance and its non-ideal capacitive behavior, respectively; R_2 is the charge transfer resistance, and CPE_2 characterizes the non-ideal capacitive behavior related to the corrosion products and the electric

double layer. As can be seen from the fitted data in Table 3, the Rs values of the various samples differ only slightly, and the goodness-of-fit χ^2 values are all on the order of 10^{-3}, indicating that the equivalent circuit can accurately describe the interfacial behavior of the alloy.

According to the total polarization resistance and the capacitive arc radius in the Nyquist plot, the total impedance of the samples in the various states ranks from high to low as follows: 500 °C > 400 °C > 350 °C > 450 °C. However, the total impedance reflected by EIS and the corrosion current density (I_{corr}) from the potentiodynamic polarization curves do not exhibit a strictly linear inverse relationship. This discrepancy reflects the competition and coupling between the barrier effect of the surface film and the localized corrosion kinetics of the matrix under different hot deformation states. Similarly, Deng et al., in a comparative study of pure Al and 2A97, 6061, 7050, and 2024 aluminum alloys, also found a conflict between the corrosion resistance ranking based on EIS frequency characteristics and that based on I_{corr}, indicating that a single electrochemical indicator is insufficient to fully characterize the corrosion resistance of aluminum alloys[22].

Combining the parameters in Table 5 for an in-depth analysis of the microstructural mechanisms of the samples in various states: the 400 °C sample exhibits the largest charge transfer resistance (R_2 = 1167 Ω·cm^2), indicating that the microstructural uniformity at this temperature is relatively good, the precipitates are fine and dispersed, and grain-boundary segregation is weak, so the driving force for microgalvanic corrosion is the smallest and the actual anodic dissolution reaction at the matrix interface is most strongly inhibited, which is consistent with its lowest I_{corr}. The 500 °C sample has the highest passive film resistance (R_1 = 3848 Ω·cm^2), which is attributed to the fact that high-temperature recrystallization and water quenching preserve the supersaturated solid solution, enabling a dense and continuous oxide film to form on the surface[23]; however, its R_2 value is only 687 Ω·cm^2, indicating that once the local film is damaged, the relatively high thermodynamic activity of the supersaturated solid solution state causes the interfacial charge transfer reaction to proceed rapidly. The 450 °C sample has the lowest R_1 (1609 Ω·cm^2) and R_2 (684 Ω·cm^2) among the four groups. This temperature lies in the sensitive range for second-phase coarsening, where coarse cathodic phases such as Cu-containing phases and Mg_2Si precipitate continuously along grain boundaries, which not only disrupts the continuity of the passive film but also, through the strong microgalvanic effect formed with the matrix, significantly accelerates interfacial anodic dissolution, resulting in the poorest corrosion resistance[24]. The R_1 and R_2 of the 350 °C sample are both intermediate, and the weak inductive loop in the low-frequency region further confirms that the local passive film is in an unstable state with a relatively high susceptibility to pitting initiation[25].

In summary, the EIS parameters supplement the conclusions of the polarization curves from the perspective of interfacial physical chemistry: the excellent corrosion resistance of the 400 °C hot-compressed state originates from the strong charge transfer resistance (high R_2) brought about by microstructural homogenization; the 500 °C hot-compressed sample benefits from the dense passive film barrier (high R_1) formed by high-temperature solution treatment, but the relatively high activity of the supersaturated solid solution state makes its overall polarization current density slightly higher than that of the 400 °C sample; the 350 °C sample has an intermediate total impedance accompanied by an inductive loop, indicating a pitting tendency; and the 450 °C hot-compressed sample exhibits the poorest corrosion resistance because second-phase coarsening degrades both the film barrier and the interfacial barrier.

Table 5. EIS fitting parameters.

Alloy condition	R_s （$\Omega \cdot cm^2$）	Q_1 ($\Omega^{-1} \cdot s^n \cdot cm^{-2}$)	n_1	R_1 （$\Omega \cdot cm^2$）	Q_2 ($\Omega^{-1} \cdot s^n \cdot cm^{-2}$)	n_2	R_2 ($\Omega \cdot cm^2$)	χ^2
350℃	65.24	6.43×10^{-6}	0.74	2276	2.13×10^{-3}	0.84	806.1	3.70×10^{-3}
400℃	67.90	8.44×10^{-6}	0.74	2668	5.09×10^{-4}	0.61	1167	5.03×10^{-3}
450℃	65.26	4.72×10^{-6}	0.78	1609	7.79×10^{-4}	0.46	684	3.58×10^{-3}
500℃	77.54	7.92×10^{-6}	0.70	3848	2.59×10^{-3}	0.83	687	5.24×10^{-3}

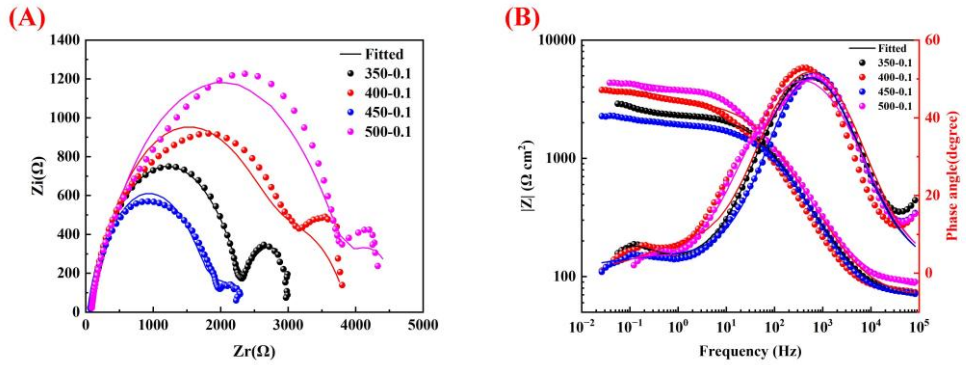


Fig. 7. EIS plots of the alloy at different temperatures: (A) Nyquist plot; (B) Bode phase angle plot.

3.2 Intergranular Corrosion Test Results

Fig. 8 presents the corrosion cross-sectional morphology of the alloy after rolling and T6 heat treatment. All three groups of specimens are dominated by localized corrosion, but differences exist in corrosion depth and morphology. In Fig. 9(A), the corrosion is relatively shallow and the corrosion front is relatively flat; Fig. 9(B) shows obvious localized deep pits, with corrosion advancing intensively from the surface toward the interior of the matrix, and undissolved particulate residues are visible at the bottom of the pits; the corrosion depth in Fig. 9(C) lies between those of the other two, mainly manifesting as local detachment of the surface film and relatively wide shallow surface exfoliation.

The above cross-sectional differences reflect the electrochemical heterogeneity of the alloy microstructure after rolling and T6 treatment. In strongly corrosive media containing Cl^-, locally continuous or semi-continuous precipitated second phases and the matrix form relatively strong microgalvanic corrosion couples[26]: the second phases act as cathodes, and the surrounding matrix acts as the anode and dissolves preferentially, thereby promoting the formation of the deep pitting shown in Fig. 9(B). Meanwhile, the local stress concentration and grain-boundary compositional segregation induced by T6 treatment weaken the continuity of the surface passive film, making it easy for Cl^- to accumulate at film defects and driving the pits to propagate inward. These cross-sectional features are consistent with the local breakdown of the passive film and the pitting initiation tendency indicated by the inductive loop in the low-frequency region of the EIS discussed above, and can also explain the abrupt increase in local current density in the anodic branch of the polarization curves. Although rolling + T6 treatment can refine the grains to a certain extent, the galvanic effect of locally precipitated phases gives the corrosion morphology pronounced localized characteristics, indicating that the alloy in this condition has a relatively high susceptibility to pitting in service environments.

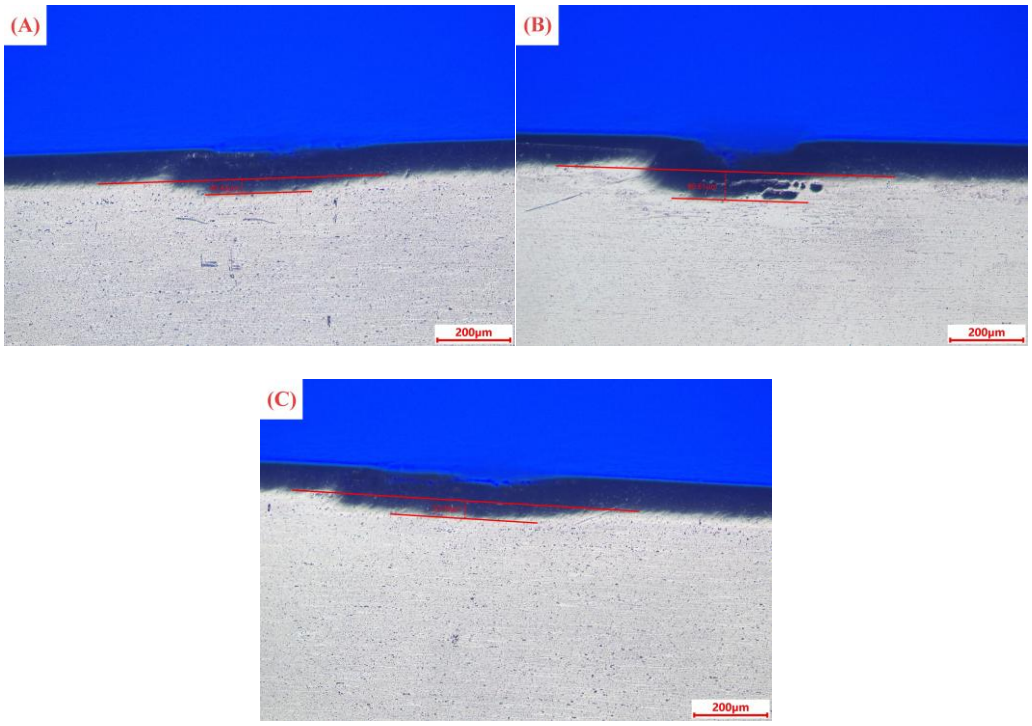


Fig. 8. Cross-sectional morphology of the alloy after intergranular corrosion.

4. Conclusions

The as-cast microstructure of alloy Y in this study is dominated by the α-Al matrix, with Cu-containing Q phase, primary Mg_2Si phase, and constituent phases such as $Al_5(Fe,Mn,Cr)Si$ and $Al_8(Fe,Mn,Cr)_2Si$ distributed at grain boundaries and within grains. After two-stage homogenization, fine dispersed precipitates such as Al(Fe,Mn,Cr)Si, Mg_2Si, and AlCuMgSi form; these precipitates can not only inhibit grain coarsening and alleviate grain-boundary segregation but also constitute microgalvanic corrosion sites due to their potential difference from the matrix.

According to the potentiodynamic polarization curves, the corrosion resistance of alloy Y under different hot compression temperatures ranks from strong to weak as follows: 400 °C > 500 °C > 350 °C > 450 °C. The 400 °C specimen has the lowest I_{corr} and the best corrosion resistance, at $7.17216\times10^{-6}A\cdot cm^{-2}$; the 450 °C specimen has the highest I_{corr} and the poorest corrosion resistance, at $1.06962\times10^{-5}A\cdot cm^{-2}$.

In addition, the EIS results of the four specimens show that the total impedance ranks from high to low as follows: 500 °C > 400 °C > 350 °C > 450 °C. The 400 °C specimen has the largest charge transfer resistance R_2 (1167 $\Omega\cdot cm^2$), indicating the strongest inhibition of interfacial anodic dissolution; the 500 °C specimen has the highest film resistance R_1 (3848 $\Omega\cdot cm^2$) but a relatively low R2, indicating that interfacial reactions readily occur rapidly once the local film is damaged; the 450 °C specimen has the lowest R_1 and R_2, indicating the poorest film and interfacial barriers; and the 350 °C specimen exhibits a small inductive loop in the low-frequency region, indicating local instability of the passive film and a tendency toward pitting initiation.

After rolling + T6 treatment, the intergranular corrosion of the alloy is dominated by localized corrosion, with cross-sectional features including shallow surface corrosion, localized deep pits, and film detachment. In Cl^--containing media, locally precipitated second phases and the matrix form microgalvanic couples, with the second phases acting as cathodes and promoting anodic dissolution of the surrounding matrix; the local stress concentration and grain-boundary

segregation induced by T6 treatment weaken the continuity of the passive film, making it easy for Cl^- to accumulate at defects and driving pitting propagation inward.

Taken together, the above analysis indicates that the 400 °C hot deformation condition enables alloy Y to achieve relatively optimal comprehensive corrosion resistance, and practical hot processing should avoid the 450 °C sensitive temperature range for second-phase coarsening; although 500 °C is favorable for forming a dense passive film, the localized corrosion risk associated with the relatively high activity of the supersaturated solid solution state must be balanced. The corrosion resistance control of high-strength and high-toughness 6xxx-series aluminum alloys for agricultural applications should synergistically optimize the hot deformation temperature, the size and distribution of precipitates, and the grain-boundary state, so as to reduce the driving force for microgalvanic corrosion and the pitting susceptibility while ensuring strength and toughness.

Conflict of interest The authors declared that they have no conflicts of interest to this work.
Funding This work was supported by the Science and Technology Innovation Enhancement Project of Shanxi Agricultural University (Project No. CXGC202412) .
Data availability The data of this study are available from the corresponding author upon reasonable request.
Author Contributions Xiaoguo Wang: Conceptualization, Methodology, Writing-original draft preparation; Hongxian Wang: Investigation,Writing-original draft preparation; Weigang Xue: Writing-review and editing; Jialin Wang: Writing-review and editing; Dongwen Guo: Writing-original draft preparation; Ruirui Wu: data curation; Weiqi Yan: Supervision, conceptualization.

5. References

[1] Chen X Z, Song Y T, Liu F Y, et al. Connotation and technical system of green design for agricultural machinery equipment[J]. Journal of Mechanical Engineering, 2025, 61(19): 290–298.

[2] Lü X Y. Development of aluminum alloy pipes for agricultural sprinkler irrigation[J]. Light Alloy Fabrication Technology, 2002, (2): 34–37.

[3] Zheng S Y. Improving the wear resistance of aluminum alloy pulleys for self-propelled agricultural machinery[J]. Grain, Oil Processing and Food Machinery, 1984, (12): 56–58.

[4] Belov A F, Hong Y X. Application of light alloys in agriculture[J]. Light Alloy Fabrication Technology, 1986, (8): 19–23, 32.

[5] Qilaika E J, Hake H P, Zhao Y Q. Corrosion of aluminum alloys with exfoliation-resistant tempers after two-year exposure in a marine environment[J]. Foreign Ship Technology (Materials), 1979, (1): 1–10.

[6] Lancaster L, Lung M H, Sujan D. Utilization of agro-industrial waste in metal matrix composites: towards sustainability[C]//Proceedings of the World Academy of Science, Engineering and Technology. 2013: 1136–1144.

[7] Zhang Q, Li J, Wang Z. In-situ observation of pitting corrosion of 6061 aluminum alloy in 3.5% NaCl solution by AFM[J]. Electrochimica Acta, 2021, 387: 138567.

[8] Li X, Chen J, Zhang H. Quantum chemical calculation and electrochemical study on intergranular corrosion mechanism of 6063 aluminum alloy[J]. Journal of Electroanalytical Chemistry, 2019, 847: 113345.

[9] Li L, Wang Q, Zhang L. Corrosion behavior of 5052 and 6061 aluminum alloys in the deep-sea environment of the South China Sea[J]. Acta Metallurgica Sinica, 2013, 49(2): 143–150.

[10] Wang H, Li Z, Chen F. Pitting corrosion behavior of 6061 aluminum alloy in deep-sea environment[J]. Deep Sea Research Part I: Oceanographic Research Papers, 2021, 172: 103589.

[11] Liu Y, Zhang L, Li M. Stress corrosion cracking behavior of 6082 aluminum alloy under different aging conditions[J]. Materials Science and Engineering: A, 2020, 792: 139876.

[12] Cui P L. Study on composition optimization, microstructure and properties of 6005 aluminum alloy[D]. Shenyang: Northeastern University, 2015.

[13] Liu H, Liu Y H, Zhao G, et al. Effects of Mn on constituents of Al-Mg-Si-Cu alloys[J]. Transactions of Nonferrous Metals Society of China, 2004, (11): 1906–1911.

[14] Zhang X M, Ke B, Tang J G, et al. Effects of Mn content on microstructure and mechanical properties of 6061 aluminum alloy[J]. Chinese Journal of Materials Research, 2013, 27(4): 337–341.

[15] Yang C Y, Lee S L, Lee C K, et al. Effects of Be and Fe on the mechanical and corrosion behaviors of A357 alloys[J]. Materials Chemistry and Physics, 2005, 93(2): 412–419.

[16] Zhu L, Guo M X, Li G J, et al. Enhancing the intergranular corrosion resistance and mechanical properties of Al–Mg–xSi–Cu–Zn alloys by synergistic intergranular and intragranular precipitation behaviors[J]. Journal of Materials Science, 2022, 57(30): 14490–14510.

[17] Wang Z X, Chen P, Li H, et al. The intergranular corrosion susceptibility of 2024 Al alloy during re-ageing after solution treating and cold-rolling[J]. Corrosion Science, 2017, 114: 156–168.

[18] Kairy S K, Rometsch P A, Davies C H J, et al. On the intergranular corrosion and hardness evolution of 6xxx series Al alloys as a function of Si:Mg ratio, Cu content, and aging condition[J]. Corrosion, 2017, 73(10): 1280–1295.

[19] Wang B X T, Xue K M, Yan S L, et al. Corrosion behavior of a new ultra-high-strength aluminum alloy due to high-energy defects and secondary phases[J]. Transactions of Nonferrous Metals Society of China, 2019, 29(4): 693–699.

[20] Kumari S, Wenner S, Walmsley J C, et al. Progress in understanding initiation of intergranular corrosion on AA6005 aluminum alloy with low copper content[J]. Journal of The Electrochemical Society, 2019, 166(11): 3114–3123.

[21] Cao C N, Zhang J Q. An introduction to electrochemical impedance spectroscopy[M]. Beijing: Science Press, 2002.

[22] Deng Y H, Liu J, Qiao Y, et al. Comparative investigations on the electrochemical behaviors among Al and aluminum alloys[J]. Materials Research Express, 2020, 7(11): 116510.

[23] Sun B W, Yu J H, Huang T J, et al. Effect of solution temperature on microstructure and oxidation properties of 6061-T651 aluminum alloy for semiconductor applications[J]. Heat Treatment of Metals, 2026, 51(7): 90–95.

[24] Zhong J K. Study on the influence and regulation of Al(Mn,Fe)Si dispersoid characteristics on the corrosion resistance of cast aluminum alloys[D]. Jinzhou: Liaoning University of Technology, 2026.

[25] Cai J T, Yu C, Fu J Y, et al. Effect of w(Mg)/w(Ag) on the microstructure and corrosion resistance of Al-Cu-Mg-Ag alloys[J]. Light Alloy Fabrication Technology, 2026, 54(8): 37–45.

[26] Su J X, Zhang Z, Cao F H, et al. Intergranular and exfoliation corrosion of aluminum alloys[J]. Journal of Chinese Society for Corrosion and Protection, 2005, (3): 187–192.